Journal of Materials Research and Technology 39 (2025) 7549–7561

Contents lists available at ScienceDirect

Journal of Materials Research and Technology

journal homepage: www.elsevier.com/locate/jmrt

Effect of Cr content on the mechanical behaviour of a high entropy alloy

R.J. Lancaster [a,b,*], D. Paolucci [a], C.E. Bevan [a,b], T. Abdullah [a,b], M. Ritchie [a], A. Olds [a], L. Wilkin [a], S. Mehraban [a], N.P. Lavery [a], N. Middleton [c], J. Plummer [c]

[a] *Faculty of Science & Engineering, Bay Campus, Swansea University, Swansea, SA1 8EN, UK*
[b] *Institute of Structural Materials, Bay Campus, Swansea University, Swansea, SA1 8EN, UK*
[c] *Dstl, Porton Down, Building 5, Salisbury, Wiltshire, SP4 0JQ, UK*

ARTICLE INFO

Keywords:
High entropy alloy
Shear punch testing
Mechanical properties
Microscopy

ABSTRACT

High entropy alloys (HEAs) are a relatively novel class of materials with unique properties. Unlike traditional alloys, which are typically based on a single primary metal combined with smaller amounts of other elements, HEAs are composed of five or more principal elements, each usually present in significant amounts. This study investigates the influence of chromium content on the microstructure and mechanical properties of $Cr_xCoFeMnNi$ HEAs focusing on three compositions: HEA10Cr, HEA20Cr, and HEA30Cr. Using Vickers hardness and shear punch testing at both room temperature and 400 °C, the research identifies a strong correlation between increasing Cr content and enhanced strength-based properties. Contrary to conventional behaviour, grain size and secondary dendrite arm spacing exhibited limited influence, with mechanical performance instead dominated by chemical composition, lattice distortion, and elemental segregation. The HEA30Cr alloy displayed the highest hardness and shear strength, attributed to more severe lattice distortion, Cr-induced dendritic growth, and sigma phase formation. Elevated temperatures reduced strength and strain hardening due to increased dislocation mobility, though ductility remained largely unaffected. Strain rate sensitivity was found to be modest at room temperature and negligible at 400 °C. These findings underscore the critical role of Cr in tuning the mechanical response of FCC-based HEAs and highlight the need for compositional control to balance strength and ductility for high-performance applications.

1. Introduction

High entropy alloys (HEAs) are a novel alloy design strategy that deviates from the conventional design approach of using one or two primary constituents with minor additions of other elements for performance enhancement [1]. Introduced by Cantor et al. [2] and Yeh et al. [2,3] in the early 2000's, these alloys were characterised by their composition of 'multi-principal elements', consisting of five or more principal elements, each with concentrations between 5 % and 35 %. HEAs are regarded as extremely promising next-generation alloys, particularly for the aerospace and defence industries, where exceptional material performance is essential. They exhibit excellent high temperature properties [4,5], fracture toughness and electromagnetic properties [6], and oxidation and wear resistance [7,8]. Additionally, the high entropy effect promotes the formation of a single or dual solid solution phase, despite the presence of numerous principal elements [7].

In 2004, Cantor et al. [2] addressed the fact that little is known about alloys containing multiple principal elements in equiatomic proportions due to the restrictive conventional alloy development strategy. The vast array of possible combinations for producing HEAs is endless, with each combination offering unique microstructural and mechanical properties [9,10]. Therefore, gaining a deeper understanding of these variations and the microstructural-property relationship is crucial to fully realising their potential.

Since the introductory papers from Cantor et al. [2] and Yeh et al. [3], research into HEAs has increased with time, with numerous studies recognising their potential for industrial use. Among this research, the most studied composition is the equiatomic CoCrFeMnNi alloy, commonly referred to as the Cantor alloy [11]. Han et al. [12] assessed the corrosion behaviour of an ultra-fine grained (UFG) version of the Cantor alloy, finding that controlling segregation of alloying elements can improve corrosion resistance. In another study, Zeng et al. [13] reviewed the mechanical properties of the Cantor composition, observing an overall strength improvement through the addition of

---

[*] Corresponding author. Faculty of Science & Engineering, Bay Campus, Swansea University, Swansea, SA1 8EN, UK.
E-mail address: r.j.lancaster@swansea.ac.uk (R.J. Lancaster).

https://doi.org/10.1016/j.jmrt.2025.11.090
Received 23 September 2025; Received in revised form 15 October 2025; Accepted 10 November 2025
Available online 11 November 2025

other supersaturated elements. Similarly, Zhao et al. [14] evaluated the mechanical property changes caused by altering the ratios of Al to Co, identifying an optimal ratio for performance improvement and cost reduction. Several other studies have also assessed the mechanical properties of the Cantor alloy [15–18].

As defined from such sources, there is a clear correlation between the alloying elements of HEAs and their final mechanical properties, through an influence of the phase structure [13]. Property optimisation can be achieved through a fine-tuning of additional elements or adjusting atomic percentage (at.%) amounts of the existing elements. Given the numerous possible combinations for HEAs, a systematic approach is necessary to fully assess their potential. Improvements in mechanical properties have already been achieved through the design of non-equiatomic Cantor alloys, such as the investigation conducted by Farjam et al. [19]. In their study, they found that a Co-rich $Co_{50}Cr_{20}Ni_{20}Fe_5Mn_5$ HEA composition provided increased yield strength, ultimate tensile strength, and total elongation as opposed to the traditional equiatomic $Co_{20}Cr_{20}Ni_{20}Fe_{20}Mn_{20}$ Cantor HEA composition. This improvement was attributed to the presence of the HCP phase and grain boundary strengthening, both of which resulted from the increased Co concentration.

Another key element is the role of Cr, which is typically introduced to stabilise body-centered cubic (BCC) structures when added in increasing amounts. Cr tends to suppress face-centered cubic (FCC) phases, which can affect the overall mechanical properties of the alloy. In some HEAs, Cr promotes the formation of sigma (σ) phases, which can embrittle the alloy at high temperatures. Cr increases strength and hardness, especially in BCC-based HEAs. It contributes to solid solution strengthening and can refine grain size. In FCC-based HEAs, high Cr content can reduce ductility, making the alloy more brittle. Cr enhances wear resistance, making HEAs more suitable for applications involving friction and abrasion. In a previous study, Jiang et al. [20] looked at an alternative HEA system ($AlCoCr_xFeNi_{2.1}$) containing varying amounts of Cr. They found that alloys with Cr ($x > 0$) exhibit a nearly complete lamellar eutectic structure composed of FCC and B2 phases, which subsequently enhanced the hardness properties. Yet, excessive Cr can lead to embrittlement, highlighting the need for optimised Cr concentrations to balance strength and ductility. In a related study, Cui et al. [21] investigated the effects of Cr content on microstructure and mechanical behaviour of Co-free $FeCr_yNiAl_{0.8}$ HEAs. Cr was added in small quantities, ranging from 0.2 to 0.6 %. In their study, Cui et al. found that an increase in Cr content correlates with a slight rise in microhardness. Specifically, the $Cr_{0.6}$ alloy achieves a Vickers microhardness of HV459, as opposed to HV438 for $Cr_{0.2}$. Also, at 1000 °C, the $Cr_{0.6}$ alloy's yield strength surpasses that of the $Cr_{0.4}$ alloy by approximately 25 MPa whilst not experiencing a drop in ductility, demonstrating improved performance at elevated temperatures with an increase in Cr content. However, many studies thus far have focussed on small additions of Cr content (typically below 10 %) and on the high temperature oxidation behaviour of these alloys, and less so on the mechanical behaviour at elevated temperature with larger Cr additions [22–24].

Assessing the mechanical properties of HEAs presents a challenge in terms of cost and availability. These alloys are typically made from multiple high-purity elements, making them expensive. Additionally, their novelty means that obtaining material is difficult, resulting in low availability. A solution to these challenges is to utilise the shear-punch (ShP) test method. The ShP test is a mechanical experiment designed to evaluate the mechanical properties of materials when availability is limited [25]. The test method involves forcing a flat-ended punch, driven by a constant displacement rate, through a thin disc of material and into a recess of tight dimensional tolerance, inferring pure shear on the sample [26,27]. Residual deflection measurements are recorded on the underside of the disc, enabling a force-deflection curve to be generated. Given the nature of deformation observed in this test, whereby shear takes place around the edges of the punch head, corresponding shear stress values can be calculated based on equation (1):

$$\tau = \frac{F}{2\pi r_{avg} t} \tag{1}$$

Where F is the punch load and r_{avg} is the average of the radius of the punch head and the radius of the receiving hole ($r_{avg} = r_{punch} + r_{die}/2$). The resulting deformation behaviour has many similarities to a σ-ε curve from a uniaxial tensile test, such as an initial linear elastic region, a yield point, a period of plastic deformation until reaching an ultimate load followed by failure.

This paper will now look to investigate the microstructure and mechanical behaviour of the $Cr_xCoFeMnNi$ HEA system, focusing on three nominal compositions of: $Cr_{10}Co_{22.5}Fe_{22.5}Mn_{22.5}Ni_{22.5}$, $Cr_{20}Co_{20}Fe_{20}Mn_{20}Ni_{20}$, and $Cr_{30}Co_{17.5}Fe_{17.5}Mn_{17.5}Ni_{17.5}$. Mechanical properties will be derived from Vickers hardness testing and the shear punch test, both at room and elevated temperature, with results related to the microstructural features associated with each of the alloy variants.

2. Experimental methods

2.1. Materials and specimens

In this research, three nominal HEA compositions $Cr_{10}Co_{22.5}Ni_{22.5}Fe_{22.5}Mn_{22.5}$ (HEA10Cr), $Cr_{20}Co_{20}Fe_{20}Mn_{20}Ni_{20}$ (HEA20Cr), and $Cr_{30}Co_{17.5}Fe_{17.5}Mn_{17.5}Ni_{17.5}$ (HEA30Cr) were manufactured into 20 mm by 8 mm diameter cylindrical rods. The rods were manufactured from high purity rods (99.9 % Goodfellows Advanced Materials). For each alloy, approximately 10 g stoichiometric charge of elements was weighed out using an Ohaus Pioneer precision analytical balance (repeatability ±0.0001 g). The charges were melted in an alumina crucible using an Ambrell 6 kW induction heater in a glovebox under a scrubbed argon cover gas (O < 10 ppm). The melt was drop cast into a cylindrical copper die, following a process previously described in Refs. [28,29]. The induction melting ensures homogeneous alloying, and the rapid cooling in the copper die limits the formation of the sigma phase.

The cylindrical rods were then sectioned into 0.7 mm thick slices and metallographically prepared with progressively finer grit papers to the final shear punch disc dimension (0.5 mm thickness (± 5 μm) x 8 mm diameter), in accordance to the recommendations defined in the related small punch standards [30,31].

2.2. Mechanical testing

2.2.1. Vickers hardness

Vickers hardness (Hv) tests were performed on a Struers Durmain-40 machine. A series of 25 hardness indents were performed in a 5 × 5 configuration, separated by 1 mm spacing, under a force of 500 g and dwell time of 10 s.

2.2.2. Shear punch testing

Shear punch (ShP) tests were performed using a bespoke in-house designed jig assembly, as previously reported in Ref. [27]. The jig assembly locates into a 5 kN electric screw test machine and comprises of an upper (2) and lower die (4) set to clamp the miniature disc (3). For ShP testing, the diameter of the receiving hole is φ2.51 mm, as depicted in Fig. 1. Load is applied to the disc sample via a flat-ended punch of diameter φ2.49 mm ($w = 10$ μm). The die sets and punch were manufactured from Nimonic 90. The dimensions of the test equipment used for ShP testing were consistent with those employed in previous studies [26,27].

For each ShP experiment, deflection measurements were recorded from an adapted transducer rod which connects the centre of the underneath surface of the specimen to a linear variable displacement transducer (LVDT), in addition to readings of the displacement behaviour recorded from the crosshead movement and the corresponding

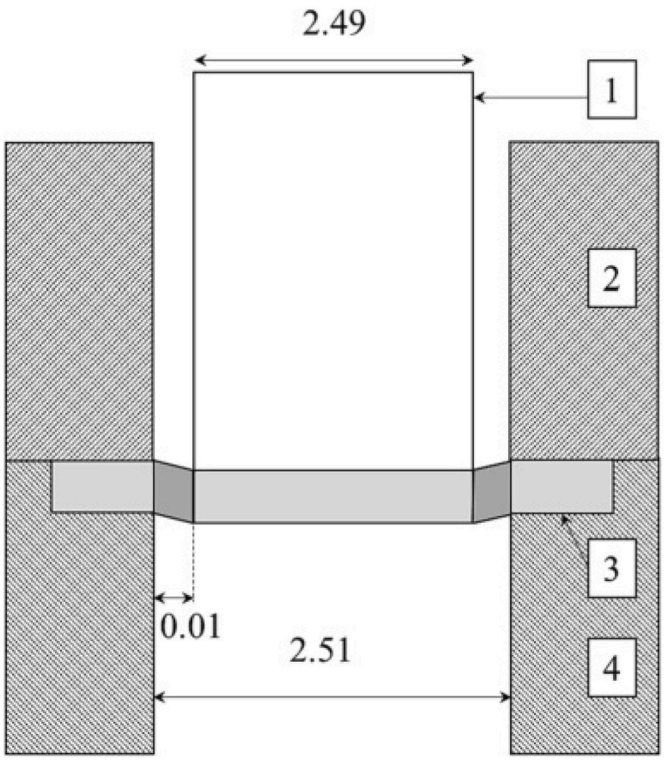

Fig. 1. Schematic illustration of the shear punch test assembly. 1 = punch, 2 = upper die, 3 = disc specimen, 4 = lower die [27].

force measurements. These values, in addition to time and force, were recorded every 0.1 s, under crosshead displacement rates of 0.2 and 10 mm min^{-1}. Each experiment was performed at either ambient room temperature or 400 °C. For elevated temperature tests, the load assembly was encased within a three-zone radiant furnace. Two N-type thermocouples were used to monitor the disc temperatures to ensure they fell within ±0.25 % of the desired test temperature in degrees Celsius, °C (for a 400 °C test, the tolerance is ±1 °C).

2.3. *Microscopy, analytical tools & simulations*

For microscopic examination, the samples were mounted in bakelite and prepared metallographically with progressively finer grit papers (400, 600, and 1200 μm). They were then polished using 6 μm and 1 μm diamond lubricants and etched with the waterless Kallings reagent (6.25 g $CuCl_2$, 125 ml HCl, 125 ml CH_3CH_2OH) for 10 s.

A Carl Zeiss Axial Observer inverted microscope was used to examine the general microstructure, including grain size, and dendrite arm spacing of the materials. The different microstructural features were measured using the mean linear intercept method through ImageJ software. For each average microstructural value documented, a minimum of 50 measurements were recorded.

A Hitachi SU3500 SEM, with electron backscatter diffraction (EBSD) capability, was used for phase determination. The phases chosen for acquisition were FCC-Ni and BCC-Fe, with the band detection mode optimised for EBSD. EBSD data was acquired using the Tango plug-in included in the Channel 5 software.

Energy Dispersive X-Ray Spectroscopy (EDX) was undertaken on the same system, using the attached Oxford Instruments SMax 50 to understand elemental distribution.

To examine the crystal structures present in the alloys following manufacture, X-ray diffraction (XRD) analysis was performed. The measurements were conducted using the Bragg-Brentano 2θ geometry with a divergent slit configuration on a BRUKER D8 Discover diffractometer. XRD. The source used was a Cu K-a source with wavelength of 1.5406 Å.

The ThermoCalc simulations were run on a 2021b version with the TCHEA5: TCS High Entropy Alloys Database.

3. Results & discussion

3.1. *Material characterisation*

3.1.1. *Phase stability*

Alloying elements such as Cr play a critical role in the stabilisation of solid solution phases in HEAs. Variations in chemical composition influence the system's compositional entropy, potentially facilitating the emergence of intermetallic or secondary phases [3]. Given that the Gibbs free energy in HEA systems is predominantly governed by entropy, a reduction in entropy corresponds to an increase in ΔG, thereby diminishing the thermodynamic stability of the solid solution. Utilising the Boltzmann equation for configurational entropy, as defined in equation (2), a comparative assessment of the three alloy compositions was conducted. The results of this analysis are summarised in Table 1.

$$\Delta S_{MIX} = -R\sum_{i=1}^{n} x_i ln x_i \tag{2}$$

Where, ΔS_{MIX} is the entropy of mixing, R is the gas constant (8.314) and x_i is the molar weight of an individual component.

The configuration of HEA30Cr exhibits the highest configurational entropy ΔS_{MIX} of 13.38 $Jmol^{-1}K^{-1}$, attributable to the uniform distribution of mole fractions among the five constituent elements. In contrast, the lowest entropy value, 13.07 $Jmol^{-1}K^{-1}$, is observed in the HEA10Cr sample. Owing to the logarithmic dependence of the Boltzmann entropy expression, reductions in the Cr content lead to a more pronounced decrease in entropy than equivalent increases.

In addition to entropy, the enthalpy of mixing (ΔH_{MIX}) is a key parameter influencing phase stability and the formation of solid solutions in HEAs. For random solid solutions to form without the precipitation of ordered or intermetallic phases, ΔH_{MIX} should typically fall within the range of −10 kJ mol^{-1} to +5 kJ mol^{-1} [32]. The enthalpy of mixing for the three alloy compositions was calculated using equation (3), with results used to assess the thermodynamic feasibility of solid solution formation [33].

$$\Delta H_{MIX} = \sum_{i=1, i\neq j}^{n} 4\Delta H_{MIX}^{ij} c_i c_j \tag{3}$$

Where ΔH_{MIX} is the enthalpy of mixing, ΔH_{MIX}^{ij} is the pairwise enthalpy of mixing and c is the mole fraction of an individual component (either i or j). ΔH_{MIX} values have been previously derived in Ref. [34]. All three alloy compositions exhibit ΔH_{MIX} values within the accepted range for single-phase solid solution formation, as shown in Table 1. The differences among the samples are minimal, with a maximum variation of only 0.10 kJ mol^{-1} between the 20 at.% and 30 at.% Cr samples. This limited variation is likely attributed to the generally mild pairwise mixing enthalpies involving Cr, including a slightly positive value for Cr–Mn interactions. More influential bonds, such as Mn–Ni (−8 kJ mol^{-1}) and Mn–Co (−5 kJ mol^{-1}), remain unaffected by changes in Cr content and contribute consistently across all compositions. Since the total enthalpy of mixing is averaged across all atomic pair interactions,

Table 1
Phase stability parameters for HEA sample compositions.

Sample ID	ΔS_{MIX} ($Jmol^{-1}K^{-1}$)	ΔH_{MIX} ($kJmol^{-1}$)	δ	*VEC*	*e/a*	Mean radius (r_{mean})
HEA10Cr	13.07	−4.14	0.82	8.25	1.68	1.378
HEA20Cr	13.38	−4.16	0.92	8	1.60	1.380
HEA30Cr	13.14	−4.06	0.98	7.75	1.53	1.383

the impact of Cr substitution is mitigated by compensatory effects from other element pairs. The HEA30Cr sample exhibits the highest (least negative) ΔH_{MIX} at -4.06 kJ mol^{-1}, making it the least energetically favourable configuration among the three. This increase is primarily attributed to the Cr–Mn interaction, the only pair in the system with a positive mixing enthalpy. In some scenarios, this could promote the formation of Cr-rich regions rather than the homogeneous solid solution typical of Cantor-type alloys [2]. Nevertheless, for the HEA30Cr composition, the calculated ΔH_{MIX} remains within the threshold where single-phase stability is still predicted.

Another parameter that can provide an indication as to whether a stable solid solution will form is the average lattice mismatch, δ, as defined in equation (4) [33]:

$$\delta = \sqrt{\sum_{i=1}^{N} c_i \left(1 - \frac{r_i}{\overline{r_i}}\right) 2} \tag{4}$$

Where δ is the average lattice mismatch, c is the mole fraction of an individual component, r_i is the atomic radii of the individual component and $\overline{r_i}$ is the average atomic radii. The atomic radii used for the calculation are listed in Table 2 (taken from Ref. [35]), while the resulting δ values for the three alloy compositions are presented in Table 1. The HEA30Cr composition exhibits the highest lattice distortion, with a δ value of 0.98. This is consistent with expectations, as Cr possesses the largest atomic radius among the constituent elements, thereby introducing greater lattice strain at higher concentrations. In contrast, the HEA10Cr alloy shows reduced distortion due to the lower Cr content and the dominance of elements with more similar atomic sizes, resulting in a higher frequency of energetically favourable non-Cr atomic pairings. Nevertheless, all δ values remain significantly below the critical threshold of 5 %, above which the formation of ordered or intermetallic phases becomes more likely [32].

While parameters such as ΔS_{MIX}, ΔH_{MIX} and δ are effective in predicting the formation of solid solution as opposed to intermetallic phases, the valence electron concentration (VEC) offers insight into the likely crystal structure of the resulting solid solution. HEAs typically crystallise into face-centered cubic (FCC), body-centered cubic (BCC), or hexagonal close-packed (HCP) structures, and the VEC value has been shown to provide a reasonably reliable indication of which structure is favoured [36]. The VEC is calculated as a weighted average of the valence electron counts of the constituent elements, as expressed in equation (5), with individual element values obtained from Ref. [36].

$$VEC = \sum_{i=1}^{n} c_i VEC_i \tag{5}$$

Where VEC is the average valence electron concentration, c is the mole fraction of an individual component and VEC_i is the valence electron concentration of an individual component. The calculated VEC values for the three alloy compositions are listed in Table 1. All values are around 8.0, suggesting that a FCC structure is favoured across the compositional range. This is consistent with empirical observations reported in the literature, which indicate that alloys with VEC $\geq$8.0 tend to stabilise in an FCC phase, while those with VEC $\leq$6.87 favour a BCC structure, and intermediate values may result in mixed or dual-phase structures [36]. The gradual increase in Cr content slightly lowers the VEC due to Cr's relatively lower valence electron count, but not enough to shift the predicted structure away from FCC. These results support the expectation that all three compositions are likely to solidify as single-phase FCC solid solutions under equilibrium conditions.

Table 2
Atomic radii of HEA elements.

Element	Co	Cr	Fe	Mn	Ni
Atomic Radii (Å)	1.25	1.28	1.27	1.26	1.25

A Hume-Rothery approach developed by Calvo-Dahlborg et al. [37–39], showed that phase data can be used to predict the most likely predominant phases (FCC, mixed or BCC). This method, built on extensive measured data points, found that HEA phases could be sorted into one of three domains based on the itinerant electrons per atom (e/a), and the mean radius of the atoms (r_{mean}). The boundaries of the three domains were i) e/a< 1.65: FCC, ii) 1.65 < e/a <2.05: mixed phases, iii) e/a >2.05: BCC. The e/a and r_{mean} values were calculated for HEA10Cr, HEA20Cr and HEA30Cr, and displayed in Table 1. According to the Hume-Rothery approach, HEA10Cr would be partly in the mixed domain (implying FCC + BCC, with low levels of BCC), but HEA20 and HEA30 would both be firmly within the FCC domain. This is to be expected with Cr as an FCC stabiliser, a finding that will be supported with XRD results (as shown later in section 3.1.4.). However, unfortunately the Hume-Rothery approach does not account for the σ phase, nor does it differentiate between multiple FCC phases.

3.1.2. *Microstructure*

Fig. 2 displays optical micrographs of the different variants from the $Cr_xCoFeMnNi$ HEA system, highlighting the microstructural evolution with increasing Cr content. Fig. 2(a) shows a relatively uniform cellular/dendritic structure, as seen in the HEA10Cr material, while HEA20Cr (Fig. 2(b)) features a fine dendritic structure characterised by short dendrite arms and minimal directionality. In contrast, Fig. 2(c) depicts the HEA30Cr microstructure which contains a significantly coarser columnar dendritic structure with elongated dendrite arms, resembling the $CoCrFeNiAl_x$ system, akin to that previously reported [40]. These notable microstructural changes across the different compositions result from several factors primarily influenced by the Cr content. Dendritic structures are commonly observed in HEA systems [41], often arising from micro-segregation during casting [42]. Additionally, Cr is known to segregate in HEAs [43], leading to non-uniform solidification rates. Cr is preferentially rejected from the growing FCC solid during dendritic solidification and solid-state diffusion is too slow during cooling to overcome those differences. Previously, Cr and Mn were shown to exhibit up-hill diffusion behaviour). That limited solid-state diffusion prevents significant homogenisation during cooling, so the as-solidified segregation pattern is retained. The result is Cr enrichment of the last to solidify liquid (interdendritic regions/grain boundaries) otherwise referred to as classic micro-segregation by solute partitioning [44]. This segregation can form Cr-rich regions that solidify at different temperatures compared to the surrounding liquid, prolonging solidification time and allowing dendrites to grow larger and more distinct. This phenomenon likely accounts for the pronounced dendrite branches and surrounding matrix seen in the HEA30Cr sample, in contrast to the more homogenised microstructures of the HEA10Cr and HEA20Cr samples.

Dendrite and secondary-dendrite arm spacing (SDAS) is a common microstructural feature that has been historically correlated with the mechanical properties of cast alloys [45]. In line with previous work [46], SDAS was measured by directly measuring the distance between adjacent secondary dendrite arms across the micrographs, using the formula given in equation (6) [46]:

$$SDAS = \frac{L}{N-1} \tag{6}$$

Where $SDAS$ is the secondary dendrite arm spacing, L is the length of the dendrite and N is the number of secondary dendrites. This approach removes any discrepancies from measuring DAS between asymmetrical dendrites, increasing the consistency of the SDAS results when compared to primary dendrite arm spacing (PDAS) measurements. A total of 25 measurements were recorded on each HEA variant, providing the mean SDAS results, which are listed in Table 3 and presented in Fig. 3. As shown, HEA10Cr exhibits the finest dendritic structure with an average SDAS value of 23.5 μm. As there is a decreased Cr content, there

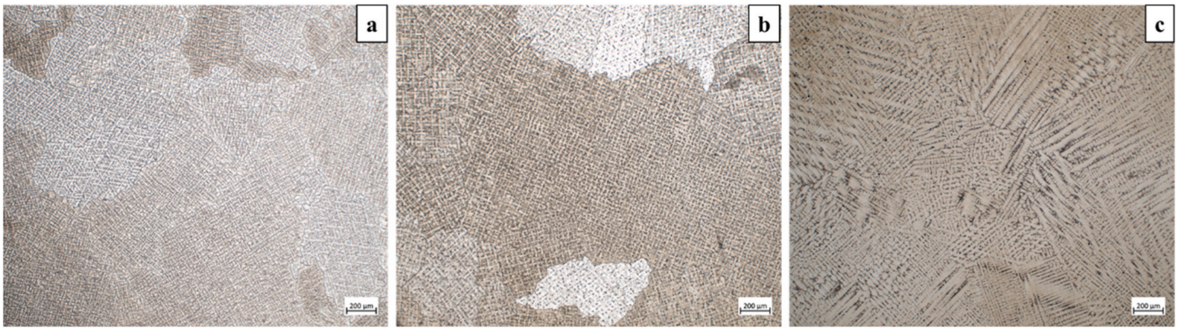

Fig. 2. Optical Micrographs of **a)** HEA10Cr, **b)** HEA20Cr and **c)** HEA30Cr, respectively.

Table 3
Average microstructural measurements of $Cr_xCoFeMnNi$ compositions, with accompanying standard deviation (SD) values.

Material	Grain area (μm^2)	*SD*	Secondary Dendrite Arm Spacing (μm)	*SD*	Dendrite Length (μm)	*SD*
HEA10Cr	108,632.8	*133,900.4*	23.5	*4.3*	170.0	*68.6*
HEA20Cr	234,243.9	*189,904.2*	30.9	*5.1*	242.5	*81.4*
HEA30Cr	788,324.6	*624,777.8*	36.1	*6.2*	348.0	*124.0*

is a greater degree of segregation into the liquid by the Mn and Ni. This segregation could result in supercooling of the liquid and a faster dendrite growth into it. The time between secondary dendrite formation would decrease, lowering the arm spacing.

The grain size of the different HEA variants was also recorded, as presented in Table 3. All three of the materials can be seen to exhibit a coarse grain size, with the HEA10Cr sample having the smallest, and HEA30Cr the largest. In all three materials, a smaller grain size is located towards the edge of the samples with significantly larger grains found in the central regions. This behaviour is due to the melt solidifying faster at the outside, inducing a high nucleation rate and thus forming finer grains. The solidification front would be slower moving towards the centre, which allows the grains to grow, also explaining their directional growth towards the centre. Very small grains can be seen propagating from the grain boundaries which are likely caused by dendrites beginning to form, then quickly becoming inhibited by the surrounding larger grains.

3.1.3. *Thermocalc*

Thermocalc predictions were performed to understand the likely phases present in final microstructures of the different HEA materials. As shown in Fig. 4, each diagram corresponds to a specific alloy composition from the CrCoFeMnNi HEA system and shows how the amounts (in molar fraction) of different phases evolve with temperature. As can be seen, HEA10Cr is mostly comprised of the FCC phase which is stable over a wide temperature range, with minimal intermetallics. Similarly, HEA20Cr, which is akin to the traditional Cantor composition, is predicted to exhibit a similar composition, where FCC is dominant and thermally stable. However, as Cr content is increased further to the HEA30Cr sample, the sigma (σ) phase is envisaged to have an increased presence, accompanied by a reduction in the FCC phase. The σ phase is an intermetallic compound that can form in HEAs, particularly under certain thermal treatments. It's typically rich in Cr and has a tetragonal crystal structure. The presence of the σ phase can influence the mechanical properties of the alloy, often leading to increased brittleness. In the CrCoFeMnNi HEA, the σ phase tends to precipitate along grain boundaries and within grains, particularly after prolonged annealing at elevated temperatures. For instance, Campari and Casagrande [47] have shown that annealing at temperatures around 1173 K for extended periods can lead to the formation and growth of σ phase precipitates. However, exposure at elevated temperature is not the only parameter that can lead to σ formation. In multicomponent systems, Cr segregation during solidification or annealing promotes local compositional inhomogeneity, which can trigger σ phase nucleation [47].

3.1.4. *Energy Dispersive X-ray spectroscopy (EDS), electron backscatter diffraction (EBSD) and X-ray diffraction (XRD)*

EDS maps of the HEA10Cr material, as given in Fig. 5, show that Co, Cr and Fe are concentrated in the dendritic cores, while the Mn and Ni

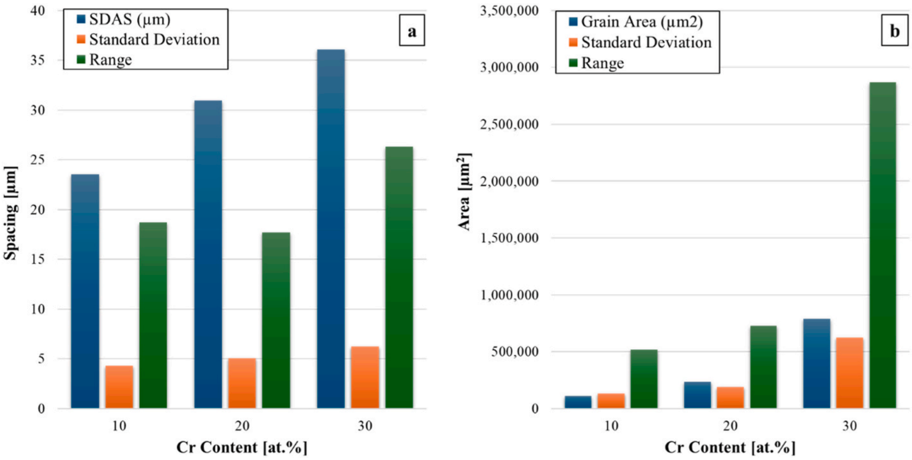

Fig. 3. Relationship between **a)** secondary dendrite arm spacing and **b)** grain size with an increased Cr content for the HEA variants.

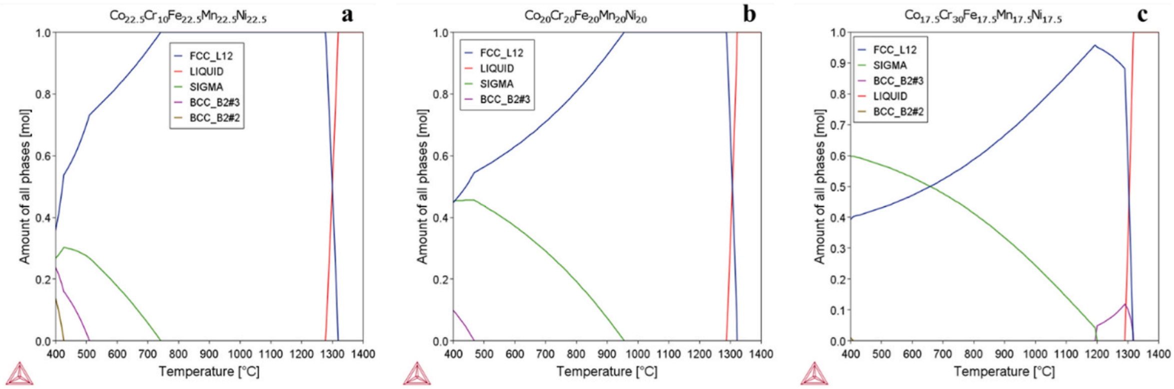

Fig. 4. Thermocalc results for **a)** HEA10Cr, **b)** HEA20Cr and **c)** HEA30Cr.

are segregated into the interdendritic sites. A very similar behaviour is observed in the HEA20Cr (Fig. 6) in terms of element segregation, but now the dendrites have coarsened due to the higher Cr content.

Of the different variants, HEA30Cr forms the coarsest dendritic structure, with an average SDAS of 36.1 μm. As the concentration of Cr is increased, the liquid in front of the solid/liquid interface may have a greater degree of constitutional supercooling, increasing the speed of dendrite growth. However, unlike the HEA10Cr and HEA20Cr (Fig. 6) samples, the increased Cr content in HEA30Cr segregates into the interdendritic regions, adding to the solute build up. This build up would decrease the growth speed of the dendrites and increase the SDAS, counteracting the supercooling effect. Fig. 7 shows that the dendrites are much wider than that of the other samples, potentially caused by the slowed growth (otherwise termed sluggish diffusion) allowing time for more atomic diffusion. Likewise, the Cr content in HEA30Cr can also be seen to be concentrated in thin needle like structures. As supported by the Thermocalc predictions, these features are likely σ.

Additionally, increasing Cr content has been linked to potential phase changes in HEAs [48–50], including the formation of high-entropy Laves phases [48,49] and a transition from a BCC phase to a dual FCC + BCC phase microstructure in the $Cr_xFeNiCu$ system [50]. Fig. 8 depicts the phase and IPF maps of the HEA30Cr material, indicating that the material composition exhibits a fully FCC microstructure.

To confirm this, X-ray diffraction (XRD) was performed on each of the HEA materials, as displayed in Fig. 9. In most publications, the equiatomic HEA20Cr alloy shows a dominant peak at (111), followed by (200) and then (220) [51], [52]. These are all FCC peaks which may imply one or more FCC phases. As can be seen in Fig. 9, the only distinct peak in the HEA20Cr material is the (200), and it is thought that this difference is due to processing. Where the as-cast (arc-remelted) or ball-milled HEA20Cr may have a peak at (111), after homogenisation at 1100 °C this can shift to (200) [53], also an FCC peak. Induction melting followed by rapid cooling in the copper dies (as used in this work) is highly successful at alloying and may have created a more stable and equilibrium end-state. It has not been possible to find XRD scans of the HEA10Cr or HEA30Cr compositions in the literature, but the results displayed in Fig. 9 suggest that the phases are predominantly (111) FCC, with this being higher for HEA10Cr than for HEA30Cr. In the current work there is no clear evidence of σ in the as-cast state, but it is suspected that prolonged heat treatment at 400–600 °C would grow the σ phase, as

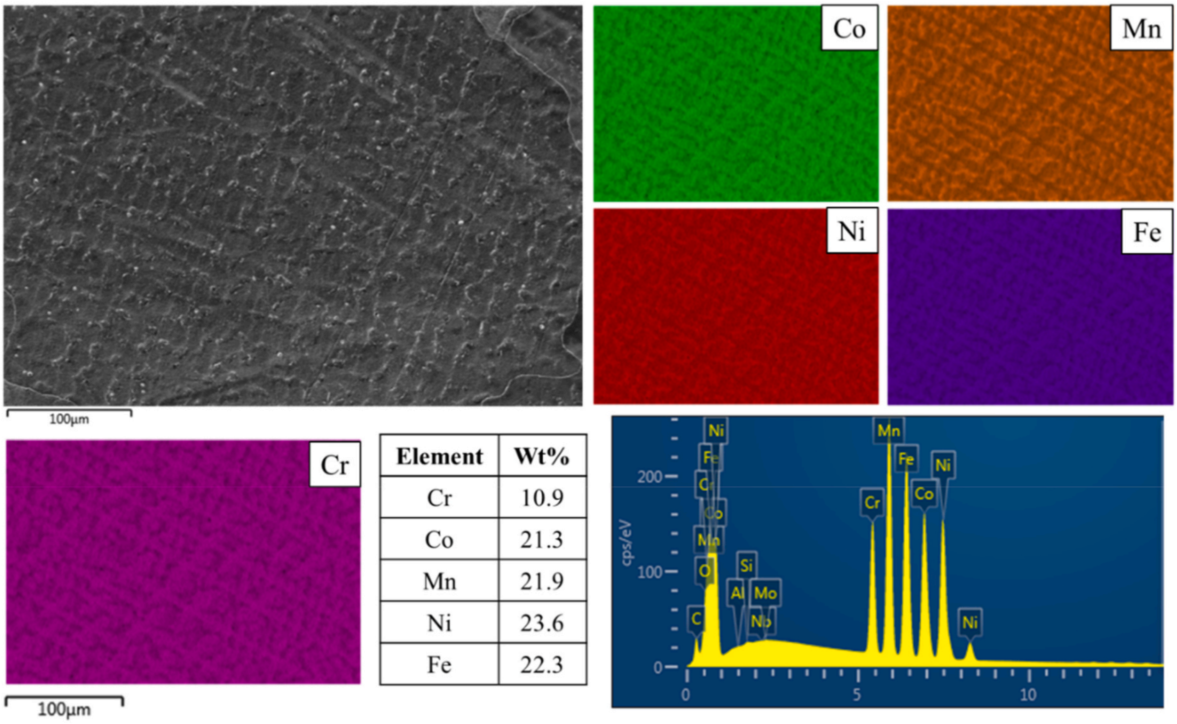

Element	Wt%
Cr	10.9
Co	21.3
Mn	21.9
Ni	23.6
Fe	22.3

Fig. 5. SEM image with the corresponding EDS elemental maps and compositional spectra of HEA10Cr.

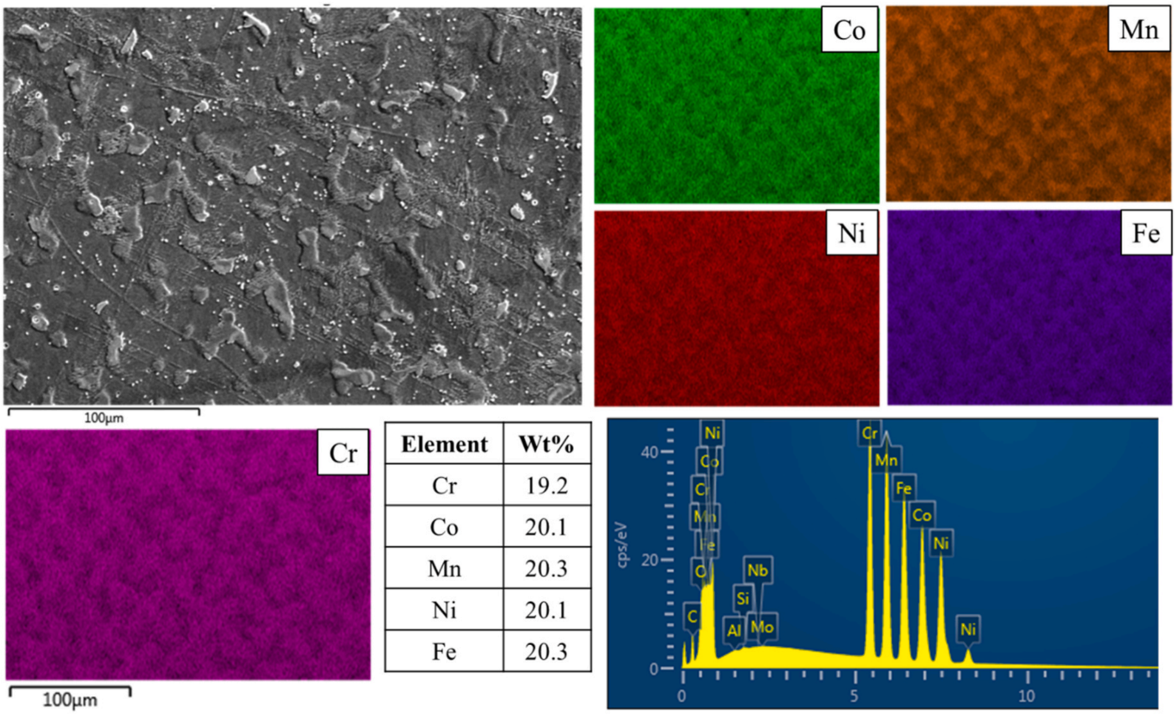

Element	Wt%
Cr	19.2
Co	20.1
Mn	20.3
Ni	20.1
Fe	20.3

Fig. 6. SEM image with the corresponding EDS elemental maps and compositional spectra of HEA20Cr.

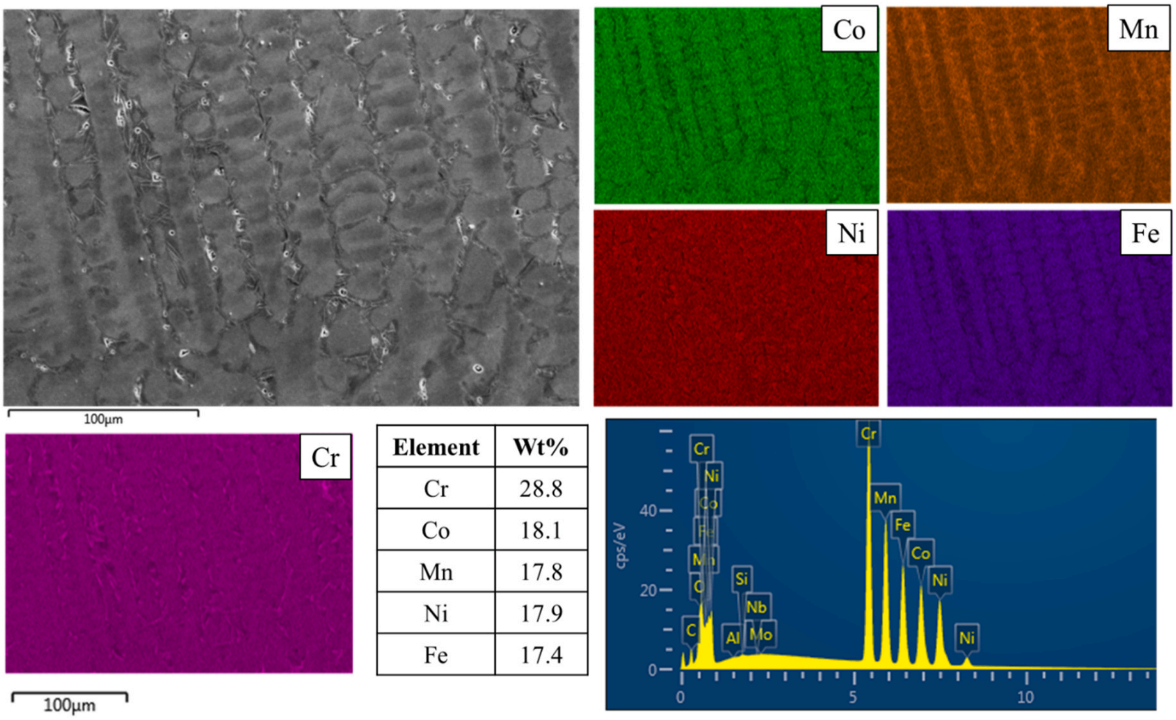

Element	Wt%
Cr	28.8
Co	18.1
Mn	17.8
Ni	17.9
Fe	17.4

Fig. 7. SEM image with the corresponding EDS elemental maps and compositional spectra of HEA30Cr.

predicted by ThermoCalc and seen in Ref. [54].

3.2. *Mechanical characterisation*

3.2.1. *Vickers hardness*

The average hardness values of the $Cr_xCoFeMnNi$ HEA variants increases significantly from approximately 158 $HV_{0.5}$ to 301 $HV_{0.5}$ with rising Cr content, as shown in Fig. 10(a)). Notably, the hardness improvement from the HEA10Cr sample to the HEA20Cr sample is approximately 20 %, while a substantial increase of 35 % occurs when Cr content rises from 20 at% to 30 at%. This marked increase in hardness for the HEA30Cr sample is likely due to enhanced solid solution strengthening at this concentration. Cr atoms have a slightly different atomic radii compared to the other elements in the CrCoFeMnNi composition [43], and their introduction at high concentrations can lead to considerable lattice distortion within the matrix. This distortion

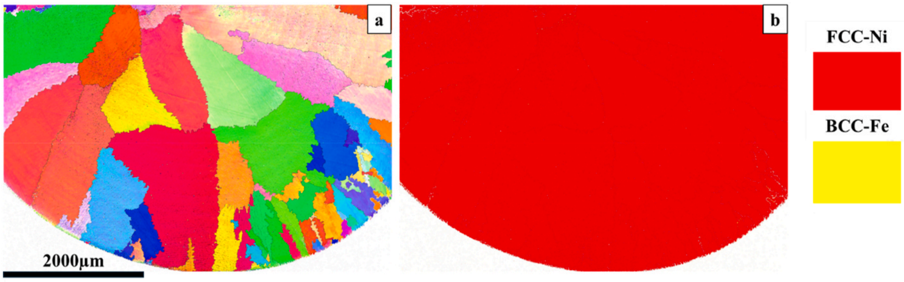

Fig. 8. EBSD generated **a)** IPF and **b)** phase maps of HEA30Cr.

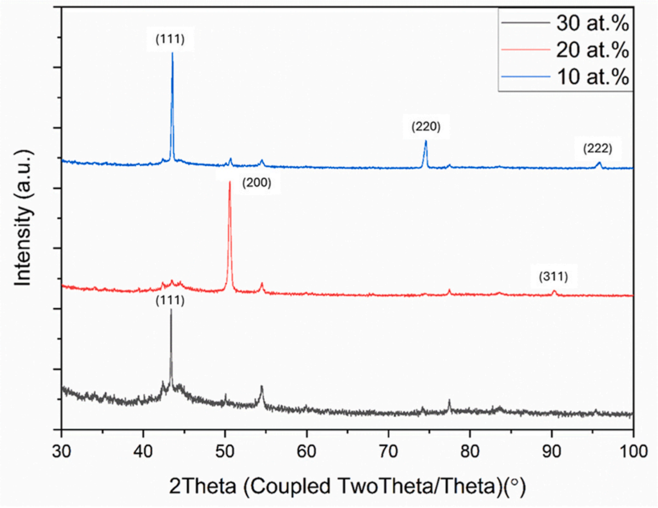

Fig. 9. XRD results for HEA materials with varying Cr content.

generates stress fields that interact with dislocations, making it more difficult for dislocations to move through the material, thereby increasing the alloy's hardness. This behaviour corroborates with the earlier findings in relation to δ, where the lattice mismatch was seen to increase with increasing Cr content (see Table 1). Numerous other HEA studies have also reported that higher Cr content correlates with increased hardness due to enhanced solid solution strengthening [49, 50]. Additionally, the elongated dendrite arms observed in the HEA30Cr sample (Fig. 2(c)) can serve as barriers to dislocation movement, leading to dislocation pileups and further contributing to the increased hardness. Also, they can also promote greater heterogeneity in the material due to the extended length of the dendrites and the difference in properties between the dendritic cores and the interdendritic regions.

Typically, according to the renowned Hall-Petch behaviour, a reduction in grain size is associated with enhanced hardness and strength due to the increased number of grain boundaries that impede dislocation movement. However, the reverse trend is seen here, since grain size has been found to increase with increasing Cr content. The reason for this lies in a combination of strengthening mechanisms. At higher concentrations, Cr is known to promote phase transformations in HEAs, which can induce hardening effects in the alloy. Geanta et al. [55] demonstrated that higher Cr concentrations in the $AlCr_xFeCoNi$ system increased the likelihood of forming intermetallic compounds that contribute to matrix hardening. Furthermore, the Cr-rich regions resulting from elevated Cr content in the $Cr_xCoFeMnNi$ HEA are known to form Cr-rich σ phases, which enhance hardness [56]. The HEA30Cr alloy also exhibits extensive dendrite growth in specific crystallographic directions, likely rich in Cr. This anisotropic behaviour of the $Cr_{30}Co_{17.5}Fe_{17.5}Mn_{17.5}Ni_{17.5}$ alloy, attributed to these crystallographic regions, also contributes to its improved hardness properties. However, as shown in Fig. 11, as Cr content increases, so does the range of grain size and hardness values. Again, this could be a result of the elemental components causing anisotropy within the structure and a higher degree of variation in the results. Yet, a more important factor to consider here is the location of the hardness indents. The dendritic cores are expected to exhibit significantly greater ductility compared to the Cr-enriched interdendritic regions, which results in elevated hardness values within the interdendritic areas and comparatively lower hardness in the dendritic cores.

The microstructural heterogeneity introduced during solidification

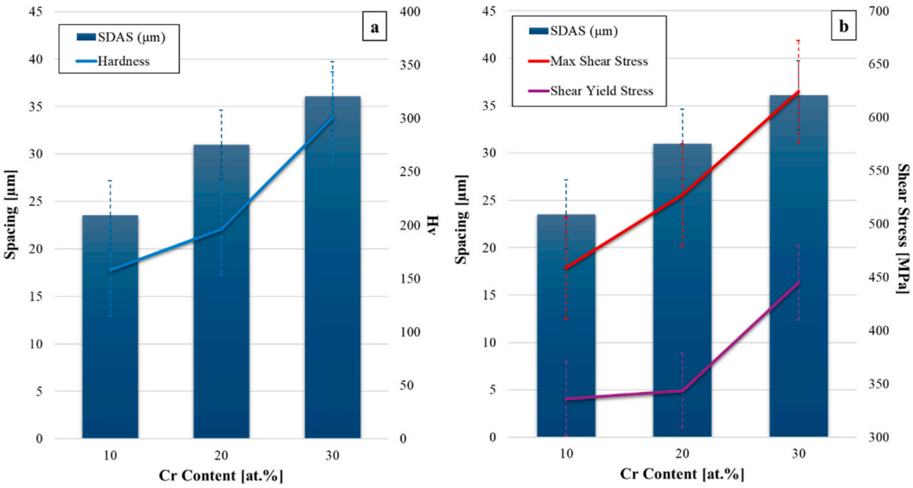

Fig. 10. Influence of secondary dendrite arm spacing on the **a)** Vickers hardness and **b)** shear punch stress properties (generated at 0.2 mm min^{-1} and 20 °C) for the HEA materials with varying Cr content.

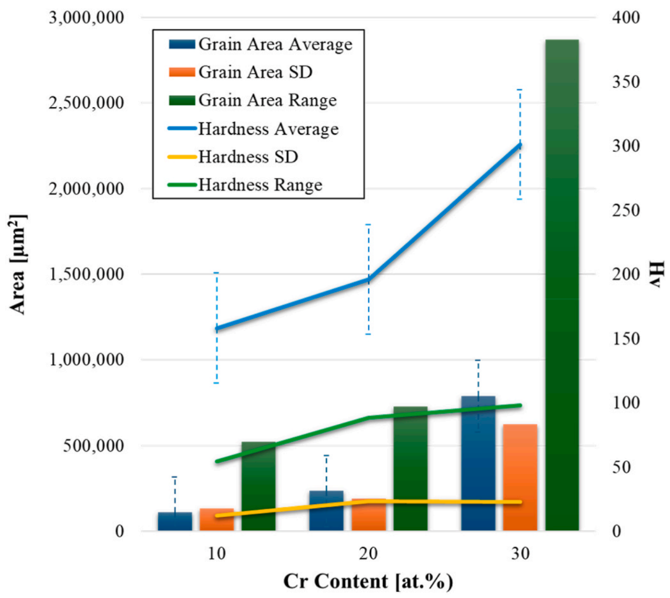

Fig. 11. Influence of grain size on the Vickers hardness properties for the HEA materials with varying Cr content. Also illustrated are the range and standard deviation values for both measures.

has a pronounced influence on the mechanical behaviour of HEAs. In particular, segregation of Cr during solidification can lead to the formation of Cr-enriched interdendritic regions, while the dendritic cores remain relatively Cr-deficient [32,36]. This compositional partitioning significantly affects local mechanical properties. The dendritic cores, due to their lower Cr content, are generally more ductile and exhibit reduced hardness, whereas the interdendritic regions, enriched in Cr, tend to be more brittle and harder due to solid solution strengthening and potential precipitation of secondary phases [57,58]. As a result, microhardness mapping typically reveals elevated hardness values in the interdendritic zones and lower values within the dendritic cores. This variation contributes to mechanical inhomogeneity, which may influence crack initiation and propagation behaviour under stress, especially in cast or directionally solidified HEA systems [59].

3.2.2. Shear punch

A similar response is observed when evaluating the shear punch behaviour of the three materials. Fig. 10(b)) presents the shear stress properties generated as a function of SDAS, whilst Fig. 12 presents the corresponding shear stress – deflection curves for the three HEA variants at room and elevated temperature, under two displacement rates. At both temperatures, the increase in Cr content appears to strengthen the alloy, but to the detriment of the material's ductility. Likewise, at room temperature, when the materials are tested under a faster displacement rate (10 mm min^{-1}), all three variants exhibit a superior performance, as opposed to the slower displacement rate (0.2 mm min^{-1}), where each of the materials are more ductile.

This behaviour follows a similar finding previously stated by Shabani et al. where the mechanical response of CrCoFeMnNi HEAs was significantly influenced by strain rate. Shabani et al. reported that as strain rate increased, so did strength but to the detriment of ductility [60]. This behaviour is characteristic of many metallic systems but is particularly notable in HEAs due to their sluggish diffusion, lattice distortion, and compositional complexity, which collectively influence dislocation motion. At low to moderate strain rates (e.g., $\sim 10^{-4}$ to 10^{-2} s^{-1}), Cantor alloys typically exhibit excellent strain hardening and ductility, attributed to a high density of forest dislocations and cross-slip mechanisms facilitated by the FCC crystal structure [61]. As the strain rate increases, dislocation motion becomes more restricted, and dynamic recovery is suppressed, leading to higher flow stresses. High strain rate testing (e.g., $\sim 10^{3}$ s^{-1}), such as via split-Hopkinson pressure bar (SHPB), has revealed a transition to a more localised deformation mode and increased yield strength [62].

Generally, the strain rate sensitivity (*m*), is low for FCC HEAs, indicating relatively rate-insensitive behaviour under quasistatic conditions. However, *m* increases slightly at elevated temperatures or very high strain rates, suggesting thermally activated dislocation processes and potential contributions from twinning or dynamic recrystallisation [63]. As seen here however, at elevated temperature (400 °C) the effect of strain rate behaviour is less clear, with each alloy variant showing limited difference across the two alternative displacement rates. Nevertheless, as depicted in Fig. 13, the shear strength properties follow a similar trend to the Vickers hardness results which all improve with an increased Cr content.

As shown in Fig. 12, at elevated temperature there is a notable drop in the strength-based properties of the different HEA compositions, despite ductility remaining relatively consistent. This is due to increased atomic mobility and dislocation recovery. Even though the solid solution strengthening remains effective at this temperature, it is counterbalanced by the thermal activation of dislocation motion. This can also be seen when considering the magnitude of strain hardening. Whereas there appears to be significant and pronounced hardening after yield at room temperature, this phenomenon is reduced at 400 °C since dislocations are able to move more freely and thus reduce the resistance to plastic flow and thereby lowering the yield strength. Furthermore, as predicted by Thermocalc, an increase in σ phase proportion is expected with an increase in Cr content, which is another factor that can play a role in the reduction of strength at elevated temperature.

The extent of strain hardening is also affected by the strain rate. At room temperature, both yield and the ultimate strength based properties increase with an increasing strain rate, yet the effect becomes less pronounced at 400 °C, where the contrasting displacement rates appear to have no significant influence on the shear stress – deflection performance. At room temperature, dislocations move primarily by

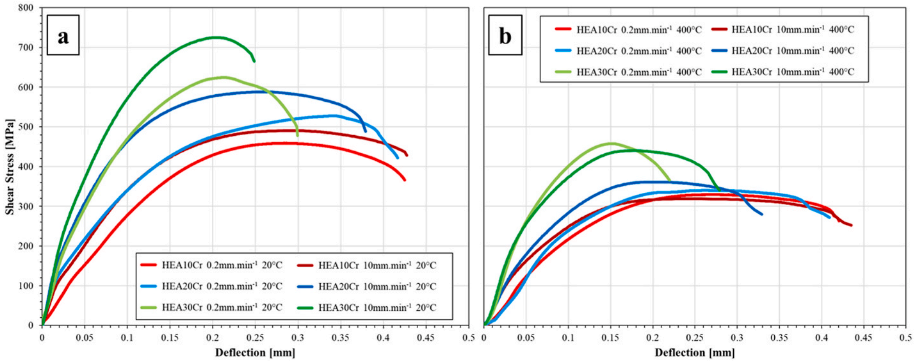

Fig. 12. Shear punch tensile behaviour of the HEA variants **a)** 20 °C, **b)** 400 °C.

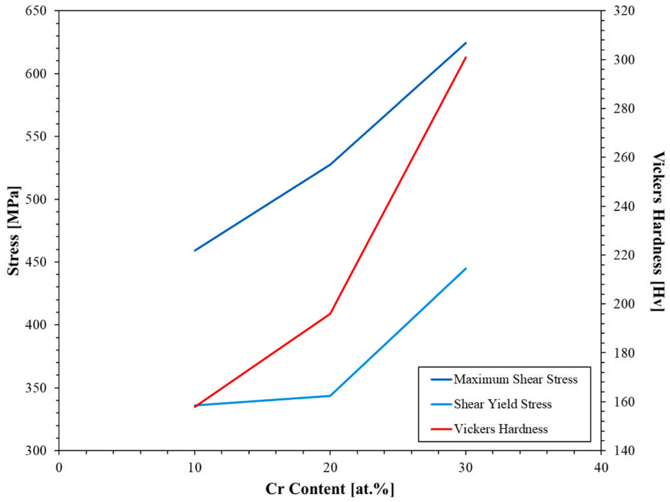

Fig. 13. Influence of Cr content on the Vickers hardness, maximum shear stress and shear yield stress behaviour of the HEA variants.

overcoming local atomic-scale obstacles, which takes time and energy. Increasing the strain rate therefore gives dislocations less time to bypass these barriers via thermal activation, resulting in higher flow stress and yield strength. Likewise, the atomic size mismatch in HEAs like CrCoFeMnNi causes lattice distortion, which already impedes dislocation glide. Then, as strain rate increases, dislocations must overcome these distorted fields more rapidly, raising the apparent flow stress.

Uniaxial properties have also previously been derived from shear punch results through a set of empirical relationships. Proof strength is determined using an offset shear yield stress (τ_{PS}). This stress is defined as the point on the shear stress (τ) – deflection (d) curve that intersects with an offset line, which is parallel to the linear portion of the curve. More details on this method can be found in Ref. [27]. The proof strength (σ_{PS}) can then be related to τ_{PS} through the following equation:

$$\sigma_{PS} = m_1 \tau_{PS} + n_1 \tag{7}$$

Likewise an estimation of σ_{UTS} values can be made from the ultimate shear stress (τ_{USS}) values generated in a ShP test through the following relationships:

$$\sigma_{UTS} = m_2 \tau_{USS} + n_2 \tag{8}$$

In each equation, m_1, m_2, n_1 and n_2 are all constants derived from linear regression across a series of results. The constants have previously been derived by Lancaster et al. [26,27], who undertook a study on a range of metallic materials with varying properties, including IN718, Ti–6Al–4V, stainless steel 316, copper and aluminium. The authors derived the various constants, whilst achieving sufficiently high R^2 values ($R^2 >$ 0.93) for the strength based parameters. The constants are $m_1 = 1.39$, $m_2 = 1.26$, $n_1 = 59.4$ and $n_2 = 56.67$.

Despite the obvious caveats of using such constants which have been derived from materials that typically deform in a considerably different manner to a HEA, indicative uniaxial properties from the ShP results were calculated, as presented in Table 4. As shown, these values also compare favourably and even surpasses those of some widely used metals and alloys in engineering applications. It should be noted however, that the constants calculated in Ref. [27] were all derived at room temperature.

The projected properties indicate that increasing the Cr content in the $Cr_xCoFeMnNi$ HEAs has been proven to have a positive effect on the overall mechanical performance, particularly by improving the tensile strength and hardness properties. The formation of dendritic structures in as-cast HEAs contributes to this enhancement by hindering dislocation motion, which strengthens the material, as noted in previous studies [64,65]. This likely explains the observed increase in strength as dendrite size expands from the HEA10Cr sample to the HEA30Cr sample. Furthermore, solid solution strengthening, which is more pronounced at higher Cr concentrations, typically results in greater strength. However, this increase in strength is accompanied by a decrease in ductility. This reduction in ductility is evident in the ShP curves shown in Fig. 10, where samples with higher Cr content exhibit less deflection under shear loading. Studies have shown that when Cr content exceeds ~30 at.%, interdendritic segregation during solidification promotes σ-phase formation, degrading ductility and toughness. Likewise, as reported earlier, Cr has the largest atomic radius among the five elements in CrCoFeMnNi (see Table 2) and as such, increasing Cr content increases lattice distortion (δ), which subsequently impedes dislocation motion. Wang et al. [66] reported that a VEC value between 6.75 and 7.86 can also promote σ phase formation, which can result in a significant decrease in ductility due to the embrittlement caused by this phase. However, it is important to re-emphasise that caution is needed when considering these empirically derived uniaxial properties, since the original materials from which they were obtained typically deform in a highly contrasting manner to a HEA. Future correlations would be far more robust if the constants were derived from both uniaxial and shear punch tests conducted on the same HEA compositions.

Table 4
Uniaxial properties derived from ShP tests on the HEA variants compared to more established metallic materials [27] (20 °C, 0.2 mm min^{-1}).

Material	τ_{USS} (MPa)	Predicted σ_{UTS} (MPa)	τ_{PS} (MPa)	Predicted σ_{PS} (MPa)
HEA10Cr	458.9	635.3	336.1	526.9
HEA20Cr	527.5	721.8	343.8	537.5
HEA30Cr	624.3	843.9	444.8	678.1
Ti–6Al–4V [27]	674	907	572	855
SS316L [27]	661	890	415	637
Copper [27]	212	323	180	310
Aluminium [27]	77	153	72	160
In718 [28]	648	874	305	484

4. Summary

As revealed in this research, the mechanical behaviour of $Cr_xCoFeMnNi$ HEAs does not follow conventional trends observed in more established material systems. From a series of hardness and shear punch tests, the inverse is true in regards to the influence of microstructural features. Whereas traditionally, the vast majority of metallic materials follow the Hall-Petch relationship, as revealed here, microstructural parameters such as grain size and secondary dendrite arm spacing have little to no influence on the mechanical performance of HEAs. Instead, the chemical composition and the segregation and distribution of elements has a significantly greater role.

As shown, all three compositions had a similar ΔH_{MIX} value, sitting within the range where single phase stability is predicted. This was evidenced by the EBSD maps, which showed that despite the HEA30Cr sample exhibiting the highest (least negative) ΔH_{MIX} value at −4.06 kJ mol^{-1}, the microstructure still consisted of a single FCC phase, akin to the HEA10Cr and HEA20Cr samples. Of greater importance was the average lattice mismatch, which was shown to be highest in the HEA30Cr material due to the greater Cr content and the larger atomic radius that Cr has amongst the other constituents. In contrast, the HEA10Cr alloy composition exhibited reduced distortion due to the lower Cr content and the dominance of elements with more similar atomic sizes. With a more severe lattice distortion, dislocations require more energy and find it more difficult to move. This significantly reduces dislocation mobility, thus, greatly strengthening the alloy.

Another key factor is the behaviour of Cr, which segregates in HEAs leading to non-uniform solidification rates. This can promote Cr rich regions that solidify at different temperatures compared to the surrounding liquid, prolonging solidification time and allowing dendrites to grow larger and more distinct. Likewise, as the concentration of Cr is increased, it promotes sluggish diffusion as it segregates into the interdendritic regions, thereby allowing more time for the dendrites to grow. This can lead to heterogeneous structures, as observed by the evolving microstructures from the outer regions of the samples, which are dominated by smaller refined grains, which gradually become larger and more elongated through directional growth towards the centre. This behaviour is coupled with elongated dendrite arms with increasing Cr content, which can serve as barriers to dislocation movement, leading to dislocation pileups and further contributing to more enhanced properties. The dendritic cores typically exhibit significantly greater ductility compared to the Cr-enriched interdendritic regions, which results in elevated hardness values within the interdendritic areas and comparatively lower hardness in the dendritic cores. As such, a higher SDAS measure would enhance hardness, as seen here in the HEA30Cr sample. However, this variation can contribute to mechanical inhomogeneity, which may influence crack initiation and propagation behaviour under stress, especially in cast or directionally solidified HEA systems. This is reflected in the greater range of hardness values observed in the HEA30Cr material.

The final contributing factor to the mechanical performance is the potential role of intermetallic compounds, and their increasing presence with an increase in Cr content. As identified in the thermocalc predictions and confirmed in the EDS maps, the presence of Cr-rich σ phases are found in the HEA30Cr composition. Such features can have a significant and generally detrimental effect on the material's mechanical behaviour. Composed primarily of Cr and Fe, σ depletes Cr from the matrix and poorly bonds to the FCC matrix. It can therefore act as a stress concentrator and site for fracture initiation, particularly if found to be located at grain boundaries. This can significantly reduce the alloy's corrosion resistance and ductility. However, it can also slightly improve yield strength. Since the presence of σ increases with an increase in Cr, as shown here, this appears to have benefitted the tensile behaviour of HEA30Cr, where the strength based properties are significantly higher than in the 10 at.% and 20 at.% samples. This could be due to the hard σ phase particles hindering dislocation glide, but without offering the ductile response seen in other strengthening mechanisms (such as coherent precipitates). The presence of σ phase can be suppressed by increasing the alloying content of Ni or Mn, but this depends on the desired application of the material and what properties are sought.

5. Conclusions

In this research, three variations of the Cantor HEA composition ($Cr_{10}Co_{22.5}Fe_{22.5}Mn_{22.5}Ni_{22.5}$, $Cr_{20}Co_{20}Fe_{20}Mn_{20}Ni_{20}$, and $Cr_{30}Co_{17.5}Fe_{17.5}Mn_{17.5}Ni_{17.5}$.) have been assessed via a combination of microscopic analysis, Vickers hardness testing, and shear punch testing (ShPT) to determine a relationship between the microstructure and mechanical properties. ShPT was performed under varying displacement rates and temperature conditions to investigate the role of the two parameters on the properties, and also enabled the prediction of uniaxial mechanical properties. The following conclusions can be drawn.

- The $Cr_xCoFeMnNi$ HEA system exhibits a dendritic microstructure across all compositions, with increasing Cr content promoting a microstructural development in the alloy system. This evolution was characterised by the formation of more defined and elongated dendrite arms, leading to a less homogeneous response under hardness and shear punch testing.
- Grain size, secondary dendrite arm spacing, shear strength and hardness properties were all found to increase with a greater Cr content, contravening well established theories such as Hall-Petch. Instead, the key strengthening mechanisms lie with atomic factors like lattice distortion, which increases with Cr. This distortion can hinder dislocation movement, thus acting to strengthen the alloy, as seen in the HEA30Cr composition. Other factors influencing strength based properties are chemical composition, elemental segregation and the presence of additional phases such as σ.
- Cr was found to segregate when added in higher concentrations, causing non-uniform solidification during casting. This was pronounced in the HEA30Cr alloy, with large regions of Cr-rich columnar dendrite growth. The elongated dendrites, and Cr strengthened interdendritic regions, were one of the key factors contributing to the improvements in properties observed in this alloy, but with increased heterogeneity.
- As derived from Thermocalc and EDS analysis, an elevated Cr content, particularly in the HEA30Cr alloy, has been found to promote σ phase precipitation, which enhances strength (via dislocation hindrance) but reduces ductility.
- Elevated temperature reduces strength in HEAs due to increased atomic mobility and dislocation recovery, which diminish strain hardening and plastic resistance, even though solid solution strengthening remains partially effective.
- At room temperature, a strain rate sensitivity of the $Cr_xCoFeMnNi$ HEA system has been established, becoming less pronounced at elevated temperatures. The strain rate sensitivity arises from dislocation dynamics, where faster strain rates reduce time for thermal activation and recovery, increasing dislocation density and interaction, which elevates the material's strength response.

Declaration of competing interest

The authors declare that they have no known competing financial interests or personal relationships that could have appeared to influence the work reported in this paper.

Acknowledgements

The authors would also like to thank the Welsh Government, European Regional Development Fund (ERDF), and SMART Expertise Wales for funding the Materials Advanced Characterisation Centre (MACH1), where the material was manufactured. The authors would also like to thank DSTL for funding the FATHOM project (DMEX MAR009). Mechanical tests were performed at SMaRT. Utilisation of the SEM was provided by Swansea University's Advanced Imaging of Materials (AIM) Facility, which was funded by the EPSRC (EP/M028267/1), The European Regional Development Fund through the Welsh Government (80708) and the Ser Solar project via the Welsh Government.

Data availability

The raw/processed data required to reproduce these findings cannot be shared at this time due to commercial restrictions.

References

[1] Li Y, Wang X, Shi Z, Liang J. Phase structure, microstructure, corrosion, and wear resistance of Al0.8CrFeCoNiCu0.5 high-entropy alloy. Lubricants Aug. 2023;11(9):358. https://doi.org/10.3390/lubricants11090358.
[2] Cantor B, Chang ITH, Knight P, Vincent AJB. Microstructural development in equiatomic multicomponent alloys. Mater Sci Eng, A Jul. 2004;375–377:213–8. https://doi.org/10.1016/j.msea.2003.10.257.
[3] Yeh J-W, Chen S-K, Lin S-J, Gan J-Y, Chin T-S, Shun T-T, Tsau C-H, Chang S-Y. Nanostructured high-entropy alloys with multiple principal elements: novel alloy design concepts and outcomes. Adv Eng Mater May 2004;6(5):299–303. https://doi.org/10.1002/adem.200300567.
[4] Wang M, Ma ZL, Xu ZQ, Cheng XW. Designing V NbMoTa refractory high-entropy alloys with improved properties for high-temperature applications. Scr Mater Jan. 2021;191:131–6. https://doi.org/10.1016/j.scriptamat.2020.09.027.
[5] Wang M, Lu Y, Wang T, Zhang C, Cao Z, Li T, Liaw PK. A novel bulk eutectic high-entropy alloy with outstanding as-cast specific yield strengths at elevated temperatures. Scr Mater Nov. 2021;204:114132. https://doi.org/10.1016/j.scriptamat.2021.114132.

[6] Li W, Xie D, Li D, Zhang Y, Gao Y, Liaw PK. Mechanical behavior of high-entropy alloys. Prog Mater Sci May 2021;118:100777. https://doi.org/10.1016/j.pmatsci.2021.100777.

[7] Choi JW, Kim JT, Hong SH, Park HJ, Jumaev E, Kim KB. Investigation of correlation between the microstructural characteristics and mechanical properties of (CoCuFeNi)100-Al high entropy alloys. J Alloys Compd Feb. 2023;933:167679. https://doi.org/10.1016/j.jallcom.2022.167679.

[8] Lu J, Zhang H, Chen Y, Li L, Liu X, Xiao W, Ni N, Zhao X, Guo F, Xiao P. Y-doped AlCoCrFeNi2.1 eutectic high-entropy alloy with excellent oxidation resistance and structure stability at 1000°C and 1100°C. Corros Sci Mar. 2021;180:109191. https://doi.org/10.1016/j.corsci.2020.109191.

[9] Yeh J-W. Alloy design strategies and future trends in high-entropy alloys. JOM Dec. 2013;65(12):1759–71. https://doi.org/10.1007/s11837-013-0761-6.

[10] Mahato A, Chahar S, Singh R, Bajargan G, Mula S. Compositional engineering of CoCrCuFeNiAlx high entropy alloys to achieve superior yield strength-ductility synergy. Mater Sci Eng, A Nov. 2024;915:147235. https://doi.org/10.1016/j.msea.2024.147235.

[11] Cantor B. Multicomponent high-entropy cantor alloys. Prog Mater Sci Jul. 2021;120:100754. https://doi.org/10.1016/j.pmatsci.2020.100754.

[12] Han Z, Ren W, Yang J, Tian A, Du Y, Liu G, Wei R, Zhang G, Chen Y. The corrosion behavior of ultra-fine grained CoNiFeCrMn high-entropy alloys. J Alloys Compd Mar. 2020;816:152583. https://doi.org/10.1016/j.jallcom.2019.152583.

[13] Zeng Z, Xiang M, Zhang D, Shi J, Wang W, Tang X, Tang W, Wang Y, Ma X, Chen Z, Ma W, Morita K. Mechanical properties of cantor alloys driven by additional elements: a review. J Mater Res Technol Nov. 2021;15:1920–34. https://doi.org/10.1016/j.jmrt.2021.09.019.

[14] Zhao Y, Cui H, Wang M, Zhao Y, Zhang X, Wang C. The microstructures and properties changes induced by Al:Co ratios of the Al CrCo FeNi high entropy alloys. Mater Sci Eng, A Aug. 2018;733:153–63. https://doi.org/10.1016/j.msea.2018.07.045.

[15] Abid T, Akram MA, Yaqub T Bin, Ramzan Abdul Karim M, Fernandes F, Zafar MF, Yaqoob K. Design and development of porous CoCrFeNiMn high entropy alloy (cantor alloy) with outstanding electrochemical properties. J Alloys Compd Jan. 2024;970:172633. https://doi.org/10.1016/j.jallcom.2023.172633.

[16] Klimova MV, Shaysultanov DG, Zherebtsov SV, Stepanov ND. Effect of second phase particles on mechanical properties and grain growth in a CoCrFeMnNi high entropy alloy. Mater Sci Eng, A Mar. 2019;748:228–35. https://doi.org/10.1016/j.msea.2019.01.112.

[17] Zamani MR, Mirzadeh H, Malekan M, Weißensteiner I, Roostaei M. Unveiling the strengthening mechanisms of as-cast micro-alloyed CrMnFeCoNi high-entropy alloys. J Alloys Compd Sep. 2023;957:170443. https://doi.org/10.1016/j.jallcom.2023.170443.

[18] Wang Z, Gao MC, Ma SG, Yang HJ, Wang ZH, Ziomek-Moroz M, Qiao JW. Effect of cold rolling on the microstructure and mechanical properties of Al0.25CoCrFe1.25Ni1.25 high-entropy alloy. Mater Sci Eng, A Oct. 2015;645:163–9. https://doi.org/10.1016/j.msea.2015.07.088.

[19] Farjam R, Akbari A, Nili-Ahmadabadi M, Shirazi H. Co50Cr20Ni20Fe5Mn5 high entropy alloy: overcoming the strength-ductility trade-off of cantor alloy. J Alloys Compd Mar. 2024;976:173000. https://doi.org/10.1016/j.jallcom.2023.173000.

[20] Jiang H, Li L, Wang R, Han K, Wang Q. Effects of chromium on the microstructures and mechanical properties of AlCoCrxFeNi2.1 eutectic high entropy alloys. Acta Metall Sin Nov. 2021;34(11):1565–73. https://doi.org/10.1007/s40195-021-01303-4.

[21] Cui P, Wang W, Nong Z, Lai Z, Liu Y, Zhu J. Effects of Cr content on microstructure and mechanical properties of Co-Free FeCryNiAl0.8 high-entropy alloys. Materials Apr. 2023;16(9):3348. https://doi.org/10.3390/ma16093348.

[22] Zhang Y, Wu H, Yu X, Tang D. Role of Cr in the high-temperature oxidation behavior of CrxMnFeNi high-entropy alloys at 800 °C in air. Corros Sci May 2022;200:110211. https://doi.org/10.1016/j.corsci.2022.110211.

[23] Chai W, Lu T, Pan Y. Corrosion behaviors of FeCoNiCr (X = 0, 0.5, 1.0) multi-principal element alloys: role of Cr-induced segregation. Intermetallics Jan. 2020;116:106654. https://doi.org/10.1016/j.intermet.2019.106654.

[24] Zhang W, Ye X, Xu D, Liu C, Fang D, Li B. Microstructures and properties of CrxFeNi(3-x)Al high-entropy alloys. Appl Phys A Jan. 2022;128(1):1. https://doi.org/10.1007/s00339-021-05118-z.

[25] Stewart GR, Elwazri AM, Varano R, Pokutylowicz N, Yue S, Jonas JJ. Shear punch testing of welded pipeline steel. Mater Sci Eng, A Mar. 2006;420(1–2):115–21. https://doi.org/10.1016/j.msea.2006.01.081.

[26] Guduru RK, Darling KA, Kishore R, Scattergood RO, Koch CC, Murty KL. Evaluation of mechanical properties using shear–punch testing. Mater Sci Eng, A Mar. 2005;395(1–2):307–14. https://doi.org/10.1016/j.msea.2004.12.048.

[27] Lancaster RJ, Jeffs SP, Haigh BJ, Barnard NC. Derivation of material properties using small punch and shear punch test methods. Mater Des Mar. 2022;215:110473. https://doi.org/10.1016/j.matdes.2022.110473.

[28] Yar MA, Norrish C, Cullen JCT, Zhang L, Brown S, Underhill R, Lavery N. "Small-Scale rapid alloy prototyping of extra-low carbon steel to investigate the effects of. Cu and Cr residuals. 2022. p. 1202–13. https://doi.org/10.1007/978-3-030-92381-5_114.

[29] Farrugia D, Brown S, Lavery NP, Pleydell-Pearce C, Davis C. Rapid alloy prototyping for a range of strip related advanced steel grades. Procedia Manuf 2020;50:784–90. https://doi.org/10.1016/j.promfg.2020.08.141.

[30] EN 10371:2021 metallic materials - small punch test method. 2021.

[31] ASTM E3205-20 standard test method for small punch testing of metallic materials. ASTM; 2020.

[32] Zhang Y, Zuo TT, Tang Z, Gao MC, Dahmen KA, Liaw PK, Lu ZP. Microstructures and properties of high-entropy alloys. Prog Mater Sci Apr. 2014;61:1–93. https://doi.org/10.1016/j.pmatsci.2013.10.001.

[33] Zhang Y, Zhou YJ, Lin JP, Chen GL, Liaw PK. Solid-solution phase formation rules for multi-component alloys. Adv Eng Mater Jun. 2008;10(6):534–8. https://doi.org/10.1002/adem.200700240.

[34] Takeuchi A, Inoue A. Classification of bulk metallic glasses by atomic size difference, heat of mixing and period of constituent elements and its application to characterization of the main alloying element. Mater Trans 2005;46(12):2817–29. https://doi.org/10.2320/matertrans.46.2817.

[35] Introduction to solid state physics Charles Kittel. 2005.

[36] Guo S, Ng C, Lu J, Liu CT. Effect of valence electron concentration on stability of fcc or bcc phase in high entropy alloys. J Appl Phys May 2011;109(10). https://doi.org/10.1063/1.3587228.

[37] Calvo-Dahlborg M, Mehraban S, Lavery NP, Brown SGR, Cornide J, Cullen J, Cieslak J, Leong Z, Goodall R, Dahlborg U. Prediction of phase, hardness and density of high entropy alloys based on their electronic structure and average radius. J Alloys Compd Jun. 2021;865:158799. https://doi.org/10.1016/j.jallcom.2021.158799.

[38] Calvo-Dahlborg M, Brown SGR. Hume-rothery for HEA classification and self-organizing map for phases and properties prediction. J Alloys Compd Nov. 2017;724:353–64. https://doi.org/10.1016/j.jallcom.2017.07.074.

[39] Calvo-Dahlborg M, Dahlborg U, Brown SGR, Juraszek J. Influence of the electronic polymorphism of Ni on the classification and design of high entropy alloys. J Alloys Compd May 2020;824:153895. https://doi.org/10.1016/j.jallcom.2020.153895.

[40] Wang W-R, Wang W-L, Wang S-C, Tsai Y-C, Lai C-H, Yeh J-W. Effects of Al addition on the microstructure and mechanical property of AlxCoCrFeNi high-entropy alloys. Intermetallics Jul. 2012;26:44–51. https://doi.org/10.1016/j.intermet.2012.03.005.

[41] Niu Z, Xie Y, Axinte E, Xu J, Wang Y. Development and characterization of novel Ni-rich high-entropy alloys. J Alloys Compd Dec. 2020;846:156342. https://doi.org/10.1016/j.jallcom.2020.156342.

[42] Abbasi E, Dehghani K. Effect of Nb-C addition on the microstructure and mechanical properties of CoCrFeMnNi high entropy alloys during homogenisation. Mater Sci Eng, A Apr. 2019;753:224–31. https://doi.org/10.1016/j.msea.2019.03.057.

[43] Farkas D, Schon CG, De Lima MSF, Goldenstein H. Embedded atom computer simulation of lattice distortion and dislocation core structure and mobility in FeCr alloys. Acta Mater Jan. 1996;44(1):409–19. https://doi.org/10.1016/1359-6454(95)00145-5.

[44] Ma D, Yao M, Pradeep KG, Tasan CC, Springer H, Raabe D. Phase stability of non-equiatomic CoCrFeMnNi high entropy alloys. Acta Mater Oct. 2015;98:288–96. https://doi.org/10.1016/j.actamat.2015.07.030.

[45] Tschopp MA, Miller JD, Oppedal AL, Solanki KN. Evaluating local primary dendrite arm spacing characterization techniques using synthetic directionally solidified dendritic microstructures. Metall Mater Trans Oct. 2015;46(10):4610–28. https://doi.org/10.1007/s11661-015-2964-7.

[46] Vandersluis E, Ravindran C. Comparison of measurement methods for secondary dendrite arm spacing. Metallogr Microstruct Anal Feb. 2017;6(1):89–94. https://doi.org/10.1007/s13632-016-0331-8.

[47] Campari EG, Casagrande A. Microstructural study of CrNiCoFeMn high entropy alloy obtained by selective laser melting. Materials Aug. 2022;15(16):5544. https://doi.org/10.3390/ma15165544.

[48] Xiang C, Fu HM, Zhang ZM, Han E-H, Zhang HF, Wang JQ, Hu GD. Effect of Cr content on microstructure and properties of Mo0.5VNbTiCrx high-entropy alloys. J Alloys Compd Mar. 2020;818:153352. https://doi.org/10.1016/j.jallcom.2019.153352.

[49] He W, Zeng C, Yang W, Chen W, Ai Y. Impact of different Cr contents on microstructural evolution and mechanical behaviour of CoCrxCuFeMnNiV high-entropy alloys. J Mater Res Technol Nov. 2022;21:4577–90. https://doi.org/10.1016/j.jmrt.2022.11.072.

[50] Wu H, Huang S, Zhu C, Zhu H, Xie Z. Influence of Cr content on the microstructure and mechanical properties of CrxFeNiCu high entropy alloys. Prog Nat Sci Mater Int Apr. 2020;30(2):239–45. https://doi.org/10.1016/j.pnsc.2020.01.012.

[51] Litwa P, Hernandez-Nava E, Guan D, Goodall R, Wika KK. The additive manufacture processing and machinability of CrMnFeCoNi high entropy alloy. Mater Des Jan. 2021;198:109380. https://doi.org/10.1016/j.matdes.2020.109380.

[52] Sun M, Yang Z, Song S, Zhang J, Lu B. Effect of Cr content on microstructure, mechanical, and corrosion properties of CoCr FeMnNi high-entropy alloys fabricated by selective laser melting. Mater Char 2024;212(Jun):113949. https://doi.org/10.1016/j.matchar.2024.113949.

[53] Vaidya M, Guruvidyathri K, Murty BS. Phase formation and thermal stability of CoCrFeNi and CoCrFeMnNi equiatomic high entropy alloys. J Alloys Compd Feb. 2019;774:856–64. https://doi.org/10.1016/j.jallcom.2018.09.342.

[54] Otto F, Dlouhý A, Pradeep KG, Kuběnová M, Raabe D, Eggeler G, George EP. Decomposition of the single-phase high-entropy alloy CrMnFeCoNi after prolonged anneals at intermediate temperatures. Acta Mater Jun. 2016;112:40–52. https://doi.org/10.1016/j.actamat.2016.04.005.

[55] Geantă V, Voiculescu I, Istrate B, Vrânceanu M-D, Ciocoiu R, Cotruț CM. The influence of chromium content on the structural and mechanical properties of AlCr$_x$FeCoNi high entropy alloys. Int J Eng Res Afr Aug. 2018;37:23–8.

[56] Park N, Lee B-J, Tsuji N. The phase stability of equiatomic CoCrFeMnNi high-entropy alloy: comparison between experiment and calculation results. J Alloys Compd Sep. 2017;719:189–93. https://doi.org/10.1016/j.jallcom.2017.05.175.

[57] Lu Y, Dong Y, Guo S, Jiang L, Kang H, Wang T, Wen B, Wang Z, Jie J, Cao Z, Ruan H, Li T. A promising new class of high-temperature alloys: eutectic high-entropy alloys. Sci Rep Aug. 2014;4(1):6200. https://doi.org/10.1038/srep06200.

[58] Pickering EJ, Jones NG. High-entropy alloys: a critical assessment of their founding principles and future prospects. Int Mater Rev Apr. 2016;61(3):183–202. https://doi.org/10.1080/09506608.2016.1180020.

[59] Hasan MN, Gu J, Jiang S, Wang HJ, Cabral M, Ni S, An XH, Song M, Shen LM, Liao XZ. Effects of elemental segregation on microstructural evolution and local mechanical properties in a dynamically deformed CrMnFeCoNi high entropy alloy. Scr Mater Jan. 2021;190:80–5. https://doi.org/10.1016/j.scriptamat.2020.08.048.

[60] Shabani M, Indeck J, Hazeli K, Jablonski PD, Pataky GJ. Effect of strain rate on the tensile behavior of CoCrFeNi and CoCrFeMnNi high-entropy alloys. J Mater Eng Perform Jul. 2019;28(7):4348–56. https://doi.org/10.1007/s11665-019-04176-y.

[61] Gludovatz B, Hohenwarter A, Catoor D, Chang EH, George EP, Ritchie RO. A fracture-resistant high-entropy alloy for cryogenic applications. Science 1979; 345(6201):1153–8. https://doi.org/10.1126/science.1254581.

[62] Park JM, Moon J, Bae JW, Jang MJ, Park J, Lee S, Kim HS. Strain rate effects of dynamic compressive deformation on mechanical properties and microstructure of CoCrFeMnNi high-entropy alloy. Mater Sci Eng, A Mar. 2018;719:155–63. https://doi.org/10.1016/j.msea.2018.02.031.

[63] Laplanche G, Gadaud P, Horst O, Otto F, Eggeler G, George EP. Temperature dependencies of the elastic moduli and thermal expansion coefficient of an equiatomic, single-phase CoCrFeMnNi high-entropy alloy. J Alloys Compd Feb. 2015;623:348–53. https://doi.org/10.1016/j.jallcom.2014.11.061.

[64] Tasan CC, Deng Y, Pradeep KG, Yao MJ, Springer H, Raabe D. Composition dependence of phase stability, deformation mechanisms, and mechanical properties of the CoCrFeMnNi high-entropy alloy system. JOM Oct. 2014;66(10): 1993–2001. https://doi.org/10.1007/s11837-014-1133-6.

[65] Zhang M, Zhang L, Fan J, Li G, Liaw PK, Liu R. Microstructure and enhanced mechanical behavior of the Al7Co24Cr21Fe24Ni24 high-entropy alloy system by tuning the Cr content. Mater Sci Eng, A Aug. 2018;733:299–306. https://doi.org/10.1016/j.msea.2018.07.069.

[66] Wang XJ, Xu M, Liu N, Liu LX. The formation of sigma phase in the CoCrFeNi high-entropy alloys. Mater Res Express Jul. 2021;8(7):076514. https://doi.org/10.1088/2053-1591/ac0a5c.